Scientia Iranica F (2022) 29(6), 3603–3618

Sharif University of Technology
Scientia Iranica
Transactions F: Nanotechnology
http://scientiairanica.sharif.edu

Entropy optimization of magnetohydrodynamic hybrid nanofluid flow with Cattaneo-Christov heat flux model

M. Vijatha and P.B.A. Reddy*

Department of Mathematics, School of Advanced Sciences, Vellore Institute of Technology (VIT), Vellore, Tamil Nadu-632014, India.

Received 11 March 2022; received in revised form 3 September 2022; accepted 1 October 2022

KEYWORDS
Casson fluid;
Magnetohydrodynamic;
Cattaneo-Christov heat flow model;
Entropy generation;
Radiation.

Abstract. The proposed model represents the construction of entropy generation, heat transport, and flow characteristics of Ag-TiO_2/blood flow in a Darcy-Forchheimer stretching cylinder under the impact of Cattaneo-Christov heat flux and thermal radiation. The basic PDEs are converted into ODEs using correct similarity transformations. The 4th-order Runge-Kutta shooting system is used to solve these ODEs. Homotopy Perturbation Method (HPM) for the nonlinear system is developed for comparison purposes, and more accurate and reliable outcomes are illustrated through graphs and tables. The impacts of various factors on velocity, temperature, and entropy production are analyzed visually. The velocity profile is enhanced with larger magnetic field values, whereas the temperature profile yields inverse effect. Higher values of the Darcy-Forchheimer number enhance skin friction and heat transfer rates. In the present analysis, Ag-TiO_2 are the nanoparticles in blood that are considered as the base fluid. This investigation has its own contribution to biomedical engineering, including medicine and electronics. The mentioned nanoparticles play an essential role in nanobiotechnology, particularly in cancer therapy and nanomedicine, because these metal nanoparticles are thought to improve the photocatalytic operation in the presence of titanium dioxide-drug delivery systems, particularly when drugs are injected into the bloodstream.

1. Introduction

Two types of fluids found in nature are distinguished by their viscosity: Newtonian and non-Newtonian. In the absence of yield stress in Newtonian liquids, shear stress is comparable to shear rate. H_2O, low-concentrated alcohol and air, and motor oil are common Newtonian fluids. A vast majority of fluids in nature are non-Newtonian, i.e., their viscosity varies in response to strain rate, resulting in uncertainty in viscosity measurements. The nonlinear rheological behavior of such liquids is dominant in various fields like milk production, pharmaceuticals, fiber technology, energy storage, etc. To make a non-Newtonian fluid model, many nonlinear terms in governing differential equations exist. There are many different fluid models such as Maxwell, Eyring-Powell, Oldroyd-A, Oldroyd-B, Carreau, Jeffrey, Casson, and so on. Among them, the most important model for suspension in our everyday life is the Casson model [1], which is a plastic fluid model with numerous applications in drilling operations, food processing, metallurgy, and bio-engineering processes. Casson fluid is a shear-thinning fluid with infinite density at null rates of shear and lower yield pressure, at which zero density

*. *Corresponding author.*
E-mail address: pbarmaths@gmail.com (P.B.A. Reddy)

doi: 10.24200/sci.2022.60107.6599

and zero flow can be seen. It behaves like an elastic solid and has molecular chains connecting the particles. At significantly higher shear stress values, this model is reduced to viscous fluid. This type of Casson model also comprises the rheological impact of some other fluids, such as syrups, cosmetics, physiological fluids, foams, etc. For a detailed study on Casson nanofluid analysis, readers are referred to Ullah et al. [2] who studied MHD slip flow of Casson liquid along a nonlinear porous stretching cylinder transfused in a porous medium with chemical response, heat generation/absorption, and viscous dissipation. Alwawi et al. [3] carried out a heat transfer investigation for a Casson nanofluid ethylene glycol-based resemblance circular cylinder with MHD effect. Sakkaravarthi and Reddy [4] examined the MHD flow behavior of two-dimensional Casson hybrid nanofluid over a porous curved stretching sheet in the presence of thermal radiation. Ramasekhar and Reddy [5] investigated the entropy generation of the non-Newtonian hybrid nanofluid in a permeable rotating disk in the presence of thermal radiation, heat generation, and viscous dissipation.

MHD is used herein to control flow fluctuations in a mixed convection system. Magnetohydrodynamic mixed convective stream and its current transport possessions are of numerous applications in nuclear power plant conserving and electrical devices, drug industry, mechanical engineering, medical engineering, geophysics, magnetic drug targeting, engineering, and astrophysics. MHD is applied to attractive medication focusing, magnetic devices for all separation, cancer tumors treatment, magnetic endoscopy, and cell death induced by hyperthermia, created by a magnetic field. MHD involves the analysis of magnetic resources and behaviors of electrically conducting fluids, e.g., magneto fluids include plasmas, salt waters, liquid metals, and electrolytes [6–8]. Chamkha and Rashad observed the flow of heat transfer around an object that was very thin and had a magnetic field around it. They investigated how the flow of nanofluid around a cone would change over time in the presence of an external magnetic field. Dhanai et al. studied how nanofluid would move up on a slope. Hydromagnetic flow analysis was carried out in [9,10]. Isa et al. [11] investigated MHD mixed convection boundary layer flow of a Casson fluid bounded by a permeable shrinking sheet with exponential variation. The effect of MHD on Casson fluid with Arrhenius activation energy and variable properties was scrutinized in [12]. In their study, Shahzad et al. [13] investigated how a stretched sheet would affect the motion of MHD nanofluid in a stratified medium containing gyrotactic microorganisms. Sheikholeslami et al. [14] discussed the effect of a homogeneous magnetic field on nanofluid flow between two circular cylinders.

Current MHD applications in engineering, residential, life sciences, and industrial production have focused on the dynamics of heat transfer phenomenon. Energy generation, space cooling, biomedical applications and magnetic drug targeting, and heat conduction in tissues are used to cool nuclear reactors [15,16]. Therefore, to minimize the negative effects of MHD, researchers have simplified the singularity of heat transfer and proposed various models of heat flux. Originally, Akbar et al. [17] began this initiative using classical continuum method and established the utmost convectional heat flux classical in continuum mechanics. This model is subject to one fundamental flaw, that is, the entire system is immediately impacted by an initial disturbance. This is known as the contradiction of heat conduction and it defies the law of interconnection. In order to resolve this problem, Cattaneo [18] enhanced Fourier's law with the addition of a thermal relaxation period that could handle heat flux. Formerly, Christov [19] further modified the Cattaneo model of heat flux by subtracting it from the Maxwell-Cattaneo model. Its uniqueness was established by Tibullo and Zampoli [20]. The Cattaneo-Christov model of heat flux is critical to bioengineering and industrial progression such as hybrid power generators, heat reduction in microelectronic devices, nuclear reactors, milk pasteurization, etc. [21]. To understand Cattaneo-Christov's heat and mass flux mode, many people have paid attention to it . Another relevant study is the work of Kundu et al. [22]. Shahid et al. [23] simulated mass and heat transfer in nanoparticle flow in a Darcy-Forchheimer medium. Jakeer and Polu [24] investigated the magneto-polymer nanofluid containing gyrotactic microorganisms over a permeable sheet with the Cattaneo-Christov heat and mass flux model.

Fluid flow and heat transfer are irreversible processes that can be quantified in entropy generation equations. The second law of thermodynamics states that entropy is created, which is true. The term entropy refers to the amount of energy unavailable in a closed thermodynamic system. In 1980, the entropy production rate was introduced by Bejan [25]. Entropy is based on the Greek word entropy, which means "moving in the direction of" or "change". In the case of fluid flow systems, entropy calculation is critical because it categorizes the factors that contribute to the loss of useful energy. As a result, the thermally designed system loses its effectiveness. The production of the system can rise by reducing the number of items that make entropy. Several researchers including Khan et al. [26] and Rashidi et al. [27] investigated the entropy for nanofluid flow with convective heat transfer in different geometric configurations. Today, a few researchers are working on entropy in exclusive geometry (see [28–34]).

Thermal radiation is characterized by a range of frequencies that extend from electromagnetic waves through the visual light range to ultraviolet rays. They include light from fire or the sun as well as the heat coming from a radiator or stove. The properties of radiation in the boundary layer flow are extremely significant because of their applications in engineering, physics, and manufacturing fields such as glass production, gas-cooled nuclear reactors, polymer processing, and furnace design as well as those in astronomical technology such as aerodynamic rockets, propulsion systems, missiles, spacecraft operating at high temperatures, and power plants for interplanetary flights. These processes cannot ignore thermal radiation effect. This is called the Roseland approximation because it describes how much heat is radiated in the energy equation. According to References [35–39], we can see that the impact of thermal radiation is very strong in case of large temperature difference. Ali et al. [40] performed the mathematical investigation of natural response and non-straight radiation for magneto-get nanofluid over an extending chamber. Mitri [41] and his team investigated how sound radiation forced cylindrical particles near an inflexible boundary. Examples of viscous fluid cylinders and the characteristic radiation torque can be seen in [42]. Investigations into the convective flow and heat transmission of an incompressible viscous nanofluid past a semi-infinite vertical stretching sheet were carried out by Yahyazadeh et al. [43].

No study has previously investigated the flow of blood and hybrid nanoparticles in a porous stretchable stretching cylinder to describe medical phenomena and treatment applications. Motivated by the primary research, the current paper examines a relevant model for MHD, porous, Darcy-Forchheimer, Cattaneo-Christov heat flux, heat generation, and thermal analysis of principal blood flow in the presence of a hybrid of Ag and TiO_2 nanoparticles to find relevant applications in the case of drug delivery schemes, mainly when drugs are inoculated into the bloodstream. This is how basic Partial Differential Equations (PDEs) are changed into dimensionless ODEs using similarity transformations. These ODEs are then numerically resolved using the bvp4c built-in function and the HPM method to compare them. The effect of the specifications on the fluid velocity is depicted through graphs and associated discussions.

2. Description of the mathematical model

This study attempts to analyze the double-dimensional axisymmetric limit coating stream of incompressible Casson hybrid nanofluid radius A with a stretching cylinder. The math of the movement is booked as the x-axis is laterally with of the axis of the cylinder just s curved co-coordinate r is ordinary to the axis of the cylinder. It is accepted that the extending cylinder has the direct axial velocity $u_w(x)$, and $T_w(x) = T_\infty + T_0(x/l)$ is the wall temperature where l, U_0, and T_0 are individually, the characteristic length, reference velocity and temperature, respectively, whereas T_∞ is the encompassing temperature. Further, speed, velocity, warm and focus slip circumstances, and happening impacts are taken into account exterior surface of the cylindrical body. It is also expected that a consistent level of resistance attractive field B_0 is oppositely functional the outspread way. To overcome the unpredictability of numerical calculation, the initiated attractive field brought about by the movement of electrically directing hybrid nanofluid is ignored since it is almost the same with applied attractive field B_0 (see Figure 1). As a result of research in [44,45], the Casson fluid rheologic equation is developed as follows:

$$\frac{\partial (ru)}{\partial x} + \frac{\partial (rv)}{\partial r} = 0, \tag{1}$$

$$u\frac{\partial u}{\partial x} + v\frac{\partial u}{\partial r} = \upsilon_{hnf}\left(1+\frac{1}{\gamma}\right)\frac{1}{r}\frac{\partial}{\partial r}\left(r\frac{\partial u}{\partial r}\right) - \frac{\upsilon_{hnf}}{k}u - \frac{\sigma_{hnf}}{\rho_{hnf}}{B_0}^2 u - \frac{c_b}{\sqrt{k}}u^2, \tag{2}$$

$$v\frac{\partial T}{\partial r} + u\frac{\partial T}{\partial x} + \lambda_e\left[u^2\frac{\partial^2 T}{\partial x^2} + v^2\frac{\partial^2 T}{\partial r^2} + 2uv\frac{\partial^2 T}{\partial x \partial r} + u\frac{\partial u}{\partial x}\frac{\partial T}{\partial x} + u\frac{\partial v}{\partial x}\frac{\partial T}{\partial r} + v\frac{\partial u}{\partial r}\frac{\partial T}{\partial x} + v\frac{\partial v}{\partial r}\frac{\partial T}{\partial r}\right] = \frac{k_{hnf}}{(\rho c_p)_{hnf}}\frac{1}{r}\frac{\partial}{\partial r}\left(r\frac{\partial T}{\partial r}\right) + \frac{\mu_{hnf}}{(\rho c_p)_{hnf}}\left(1+\frac{1}{\gamma}\right)\left(\frac{\partial u}{\partial r}\right)^2 - \frac{1}{(\rho c_p)_{hnf}}\frac{\partial q_r}{\partial r} + \frac{Q_0}{(\rho c_p)_{hnf}}(T - T_\infty) + \frac{\sigma_{hnf}{B_0}^2}{\rho_{hnf}}u^2. \tag{3}$$

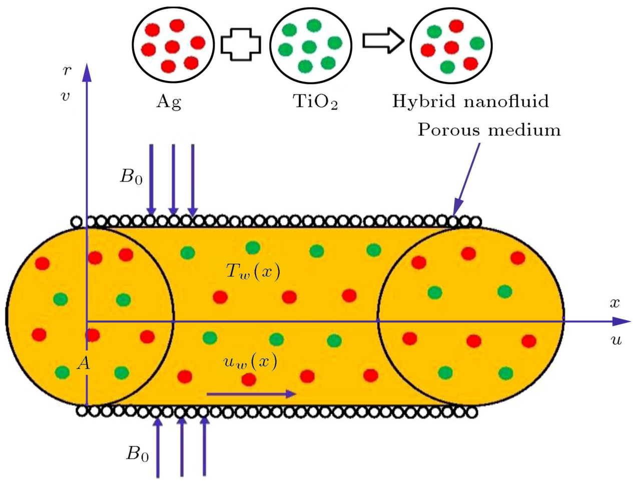

Figure 1. The flow pattern of a hybrid nanofluid.

Boundary Conditions:

$$u = u_w(x) + k_0 \upsilon_{hnf}\left(1+\frac{1}{\gamma}\right)\frac{\partial u}{\partial r},$$

$$v = v_0, \quad -k_{hnf}\frac{\partial T}{\partial r} = h_f(T_w - T_\infty), \quad \forall_x,$$

$$r = A, \quad u \to 0, \;\; T \to T_\infty, \;\; r \to \infty, \tag{4}$$

where (u,v) are the velocity components in the (x,r) directions, respectively; ρ, υ, and σ are density, kinematic consistency, and explicit warmth limit of Casson nanofluid, respectively; remains the non-Newtonian boundary; k signifies the porosity of a permeable medium; $\alpha = \alpha_\infty\{1+\varepsilon[(T-T_\infty)/\Delta T]\}$ stands for fluid flexible warm conductivity (where ε is variable warm conductivity boundary and α_∞ is the encompassing liquid warm diffusivity); v_0 is pull/blowing speed; and K_0 is speed. T_0 changes in a strictly nonlinear fashion and illustrates incomplete differential conditions into an arrangement of customary differential conditions (ODEs). We present the stream work $\psi(x,r)$ such that:

$$ru = \frac{\partial \psi}{\partial r}, \quad rv = -\frac{\partial \psi}{\partial x}. \tag{5}$$

Similarity variables are given as:

$$u = \frac{xU_0}{l}f'(\eta), \quad u_w(x) = U_0(x/l),$$

$$v = \frac{-A}{r}\sqrt{\frac{\upsilon U_0}{l}}f(\eta), \qquad \eta = \frac{r^2-A^2}{2A}\sqrt{\frac{U_0}{\upsilon l}},$$

$$\theta(\eta) = \frac{(T-T_\infty)}{(T_w-T_\infty)}. \tag{6}$$

Dimensionless variables are as follows:

$$\frac{n_1}{n_2}\left[\left(1+\frac{1}{\gamma}\right)(2\omega f'' + (1+2\eta\omega)f''')\right] - \frac{n_1}{n_2}\left(1+\frac{1}{\gamma}\right)kf' - \frac{n_3}{n_2}Mf' - Frf'^2 - f'^2 + ff'' = 0, \tag{7}$$

$$\frac{1}{Pr}\frac{n_5}{n_4}(2\theta'\omega + \theta''(1+2\eta\omega)) - \frac{1}{Pr}\frac{1}{n_4}Rd\,(2\theta'\omega + \theta''(1+2\eta\omega)) + \frac{n_3}{n_4}MEcf'^2 + \frac{n_1}{n_5}(1+2\eta\omega)Ec\left(1+\frac{1}{\gamma}\right)f''^2 - \alpha_t(ff'\theta' + \theta''f^2) + f\theta' + \frac{1}{n_4}Q\theta = 0. \tag{8}$$

Transformed boundary conditions are:

$$f(0) = s, \quad f'(0) = 1 + \left(1+\frac{1}{\gamma}\right)\delta f''(0),$$

$$n_5\theta'(0) = -Bi(1-\theta(0)) \quad \text{as} \quad \eta \to 0$$

$$f' = 1, \quad \theta = 0 \quad \text{as} \quad \eta \to 0, \tag{9}$$

where $\omega = \sqrt{\left(\frac{\upsilon_f l}{A^2 U_0}\right)}$, $1+2\omega\eta = \frac{r^2}{A^2}$, $M = \sqrt{\left(\frac{\sigma_f l B_0{}^2}{\rho_f U_0}\right)}$, $k = \frac{\upsilon_f l}{KU_0}$, $Pr = \frac{\upsilon_f}{\alpha_\infty}$, $\alpha_t = \lambda_e\frac{U_0}{l}$, $Ec = \frac{u_w{}^2}{(c_p)_f(\mathrm{T}_w-\mathrm{T}_\infty)}$ (for $u_w = U_0\left(\frac{x}{l}\right)$, the average constant value of x is considered), $s = v_0\sqrt{\frac{l}{\upsilon U_0}}$ (for suction $s>0$ or injection $s<0$), $\delta = K_0\sqrt{\frac{\upsilon U_0}{l}}$, $Bi = \frac{h}{k_f}\sqrt{\frac{\upsilon l}{U_0}}$, and $Fr = \frac{Cpx}{A\sqrt{K}}$. The mathematical types of constants n_1, n_2, n_3, n_4, and n_5 can now be communicated as follows:

$$n_1 = \frac{\mu_{hnf}}{\mu_f}, \qquad n_2 = \frac{\rho_{hnf}}{\rho_f}, \qquad n_3 = \frac{\sigma_{hnf}}{\sigma_f},$$

$$n_4 = \frac{(\rho c_p)_{hnf}}{(\rho c_p)_f}, \qquad n_5 = \frac{k_{hnf}}{k_f}. \tag{10}$$

The skin friction coefficient C_f and local heat transfer rate from Nusselt number Nu_x on the surface of the cylinder are defined as:

$$C_f = \frac{2\tau_w}{\rho u_w{}^2}, \quad Nu_x = \frac{xq_w}{k(T_w-T_\infty)}, \tag{11}$$

where surface shear stress and heat flux for Casson fluid are respectively given as follows:

$$\tau_w = \mu_{hnf}\left(1+\frac{1}{\gamma}\right)\left(\frac{\partial u}{\partial r}\right)_{r=A},$$

$$q_w = -\left(k_{hnf} + \frac{16\sigma^* T^3}{3k^*}\right)\left(\frac{\partial T}{\partial r}\right)_{r=A}. \tag{12}$$

Local temperature and mass transfer rates are given for local $Re_x = xu_w/\upsilon$ Reynolds number.

$$\frac{1}{2}\sqrt{Re_x}C_f = n_1\left(1+\frac{1}{\gamma}\right)f''(0),$$

$$\frac{Nu_x}{\sqrt{Re_x}} = -n_5(1+Rd)\theta'(0). \tag{13}$$

Entropy Generation Analysis: Entropy is defined physically as the measure of irreversibility and signifies a state of disorder in the system and its surroundings. When heat is not completely used for work, the amount of entropy it creates is known. Entropy generation is so expressed as follows:

$$S'''_{gen} = \frac{k_{hnf}}{T_\infty{}^2}\left[\left(\frac{\partial T}{\partial r}\right)^2 + \frac{16\sigma_f{}^* T_\infty{}^3}{3k^* k_f}\left(\frac{\partial T}{\partial r}\right)^2\right]$$
$$+\left(1+\frac{1}{\gamma}\right)\frac{\upsilon_{hnf}}{T_\infty}\left(\frac{\partial u}{\partial r}\right)^2$$
$$+\left(\frac{\sigma_f B_0{}^2}{\rho_f T_\infty} + \left(1+\frac{1}{\gamma}\right)\frac{\upsilon_f}{KT_\infty}\right)u^2. \tag{14}$$

Implementing Eq. (6) in Eq. (14), it becomes the dimensionless entropy generation as follows:

$$N_G = \frac{S'''_{gen}}{S'''_0} = n_5\frac{Re}{X}\alpha_1\left(1+Rd\right)\left(1+2\omega\xi\right)\theta'^2$$
$$+n_1\frac{Re}{X}Br\left(1+\frac{1}{\gamma}\right)\left(1+2\omega\xi\right)f''^2$$
$$+\frac{Re}{X}Br\left(M+\left(1+\frac{1}{\gamma}\right)k\right)f'^2, \tag{15}$$

where $N_G = \frac{s'''_{gen}}{s'''_0} = \frac{T_\infty{}^2 x}{k(T_w-T_\infty)^2}$, $S'''_0 = k(T_w - T_\infty)^2 / T_\infty{}^2 l^2$, $\alpha_1 = T_w - T_\infty/T_\infty$, $Br = \upsilon_f u_w{}^2/k\Delta T$.

The Bejan number is delineated by Eq. (16) as shown in Box I. The thermophysical parameters and comparison of the velocities that can be employed in this analysis are provided in Tables 1 and 3.

Colloidally diluted hybrid nanofluid is used in this case TiO_2-Ag nanoparticle interruptions in a base fluid (blood). Blood and Ag-TiO_2 hybrid nanoparticles are shown in Table 1 with their thermophysical properties at temperatures of 20°C–30°C, at which they work best. Table 2 shows the mathematical models of hybrid nanofluid thermophysical properties [46]. The correlations among the thermophysical properties of hybrid nano liquids including effective heat capacity $(\rho c_p)_{hnf}$, effective density ρ_{hnf}, thermal conductivity k_{hnf}, and electrical conductivity σ_{hnf} are as follows.

Density, viscosity, thermal conductivity (k), electrical conductivity (σ), heat capacity $(\rho c_p)_f$, and the electrical conductivity of the base fluid σ_f are all represented by the letters ρ, μ, C_p, and, k respectively. Solid nanogranules Ag and TiO_2 are represented by subscripts 1 and 2, respectively, the base fluid is designated as f, and hybrid nanofluids are referred to as hnf. The shape of nanoparticles can be pronounced

$$Be = \frac{n_5\frac{Re}{X}\alpha_1\left(1+Rd\right)\left(1+2\omega\xi\right)\theta'^2}{n_5\frac{Re}{X}\alpha_1\left(1+Rd\right)\left(1+2\omega\xi\right)\theta'^2 + n_1\frac{Re}{X}Br\left(1+\frac{1}{\gamma}\right)\left(1+2\omega\xi\right)f''^2 + \frac{Re}{X}Br\left(M+\left(1+\frac{1}{\gamma}\right)k\right)f'^2}. \tag{16}$$

Box I

Table 1. Thermal characteristics of nanoparticles and base fluid [46].

Physical properties	ρ (kg/m^3)	C_p (J/kg.k)	σ (1/Ωm)	k (W/mK)
Blood	1063	3594	0.8	0.492
Ag	10500	235	2.6×10^6	429
TiO_2	4250	686.2	6.30×10^7	8.9538

Table 2. Mathematical models of hybrid nanofluid thermophysical properties [46].

Properties	Hybrid nanofluid
Viscosity	$\frac{\mu_{hnf}}{\mu_f} = \frac{1}{(1-\phi_1)^{5/2}(1-\phi_2)^{5/2}}$
Density	$\frac{\rho_{hnf}}{\rho_f} = \left[(1-\phi_2)\left\{1-\left(1-\frac{\rho_{s1}}{\rho_f}\right)\phi_1\right\}+\phi_2\frac{\rho_{s2}}{\rho_f}\right]$
Electrical conductivity	$\frac{\sigma_{hnf}}{\sigma_f} = 1+\frac{3\phi\left(\phi_1\sigma_1+\phi_2\sigma_2-\phi\sigma_f\right)}{\left(\phi_1\sigma_1+\phi_2\sigma_2+2\phi\sigma_f\right)-\phi\sigma_f\left(\phi_1\sigma_1+\phi_2\sigma_2-\phi\sigma_f\right)}$
Heat capacity	$\frac{(\rho c_p)_{hnf}}{(\rho c_p)_f} = \left[(1-\phi_2)\left\{1-\left(1-\frac{(\rho c_p)_{s1}}{(\rho c_p)_f}\right)\phi_1\right\}+\phi_2\frac{(\rho c_p)_{s2}}{(\rho c_p)_f}\right]$
Thermal conductivity	$\frac{k_{hnf}}{k_{bf}} = \frac{\left(k_{s2}+(m-1)k_{bf}\right)-(m-1)\phi_2\left(k_{bf}-k_{s2}\right)}{\left(k_{s2}+(m-1)k_{bf}\right)+\phi_2\left(k_{bf}-k_{s2}\right)}$ $\frac{k_{bf}}{k_f} = \frac{\left(k_{s1}+(m-1)k_{bf}\right)-(m-1)\phi_1\left(k_{bf}-k_{s1}\right)}{\left(k_{s1}+(m-1)k_{bf}\right)+\phi_1\left(k_{bf}-k_{s1}\right)}$

by the shape parameter m, with values of $m = 4.9, 3.7$, and 5.7 corresponding to cylindrical, brick-shaped, and platelet nanoparticles, respectively. This study focuses on platelet-shaped nanoparticles with $m = 5.7$. In addition, ϕ_1 and ϕ_2 denote the total volume proportions of nanogranules distributed in the working base fluid.

3. Method for resolving the problem

3.1. Numerical procedure

The MATLAB is used to implement the list of nonlinear ODEs (Eqs. (7) and (8)) as well as the boundary conditions (Eq. (9)). To do so, the set of ODEs is first modified into ODEs of first order. The substitutes are calculated by Eqs. (17)–(19) as shown in Box II. With the boundary conditions:

$$ya\left(1\right)=s,\quad ya\left(2\right)=1+\left(1+\frac{1}{\gamma}\right)\delta ya\left(3\right),$$

$$ya\left(4\right)=-Bi\left(1-ya\left(5\right)\right),\quad yb\left(2\right),\quad yb\left(4\right). \tag{20}$$

Entropy generation is obtained by Eqs. (21) and (22) as shown in Box III. After converting the equations and boundary conditions to the first order, we can obtain our numerical findings for heat transfer rate and shear stress, respectively. The dimensionless nonlinear ordinary differential calculations are numerically solved and the velocity and temperature graphs are shown using MATLAB bvp4c. The numerical stability is shown below.

3.2. Homotopy perturbation technique analysis

The nonlinear ordinary differential equations (Eqs. (7) and (8)) along with the entropy generation (Eq. (15)) are tackled mathematically with the assistance of HPM method.

Let consider the nonlinear differential equation system below:

$$\tau\left(\varsigma\right)-f\left(x\right)=0, x\in\psi. \tag{23}$$

With regard to boundary conditions, we have:

$$A\left(\varsigma,\frac{\partial\varsigma}{\partial\eta}\right)=0, x\in\partial\psi. \tag{24}$$

$$f=y\left(1\right),\quad f'=y\left(2\right),\quad f''=y\left(3\right),\quad f'''=y'\left(3\right),\quad \theta=y\left(4\right),\quad \theta'=y\left(5\right),\quad \theta''=y'\left(5\right), \tag{17}$$

$$y'\left(3\right)=-\frac{n_2\left[\frac{2\omega n_1\left(1+\frac{1}{\gamma}\right)y(3)}{n_2}-\frac{n_3 M y(2)}{n_2}-y^2\left(2\right)+y\left(1\right)y\left(3\right)-\frac{n_1}{n_2}\left(1+\frac{1}{\gamma}\right)ky(2)-Fry^2\left(2\right)\right]}{n_1\left[\left(1+\frac{1}{\gamma}\right)\left(1+2\eta\omega\right)y\left(3\right)\right]}, \tag{18}$$

$$y'\left(5\right)=-\frac{n_4\left[\left(\frac{\begin{array}{c}2n_5\omega y\left(5\right)-2Rd\omega y\left(5\right)\\+MEcn_3\Pr y^2\left(2\right)\end{array}}{n_4}\right)+\frac{n_1\Pr Ecy^3(3)\left[\left(1+\frac{1}{\gamma}\right)(1+2\eta\omega)\right]}{n_5}+\Pr y\left(1\right)y\left(5\right)-\Pr\alpha_t y\left(1\right)y\left(2\right)y\left(5\right)+Pr\frac{1}{n_4}Q\theta\right]}{n_5\left(1+2\eta\omega\right)-n_4\Pr\alpha_t p^2\left(1\right)-Rd\left(1+2\eta\omega\right)}. \tag{19}$$

Box II

$$N_G=n_5\frac{Re}{X}\alpha_1\left(1+2\eta\omega\right)\left(1+Rd\right)y''\left(5\right)+n_1\frac{Re}{X}Br\left[\left(1+\frac{1}{\gamma}\right)\left(1+2\eta\omega\right)y''^2\left(3\right)\right]$$
$$+y'^2\left(2\right)Br\frac{Re}{X}\left(M+\left(1+\frac{1}{\gamma}\right)k\right), \tag{21}$$

$$Be=\frac{n_5\frac{Re}{X}\alpha_1\left(1+2\eta\omega\right)\left(1+Rd\right)y''\left(5\right)}{\begin{array}{l}n_5\frac{Re}{X}\alpha_1\left(1+2\eta\omega\right)\left(1+Rd\right)y''\left(5\right)+n_1\frac{Re}{X}Br\left[\left(1+\frac{1}{\gamma}\right)\left(1+2\eta\omega\right)y''^2\left(3\right)\right]\\+y'^2\left(2\right)Br\frac{Re}{X}\left(M+\left(1+\frac{1}{\gamma}\right)k\right).\end{array}} \tag{22}$$

Box III

In this case, $\partial\psi$ represents the domain's boundary, $f(x)$ is the arithmetic function, and $\tau(\zeta)$ is the operator for nonlinear differential equations. Moreover, the boundary operator is denoted by the letter A. P can be generally divided into two parts: Nonlinear N and linear L.

$$f(x) = L(\varsigma) + N(\varsigma). \tag{25}$$

The HPM structure is given as follows:

$$H(\varsigma, p) = (1-p)\left[L(\varsigma) - L(\varsigma_0)\right] + p\left[\tau(\varsigma) - f(\varsigma)\right] = 0, \tag{26}$$

where:

$$\tau(x, p) : \psi \times [0,1] \rightarrow R_1. \tag{27}$$

$p \in [0,1]$ is a parameter for implanting and ς_0 is the basic estimate of Eq. (23), which captures the boundary conditions.

The solution given above can be written as a power series in p:

$$\varsigma = \varsigma_0 + p\varsigma_1 + p^2\varsigma_2 + \cdots\cdots$$

$p = 1$ is the closest approach to the solution.

$$\varsigma = \varsigma_0 + \varsigma_1 + \varsigma_2 + \cdots\cdots.$$

3.3. HPM method implementation

In this section, the HPM method is used to solve nonlinear ODEs (Eqs. (7) and (8)). With the boundary condition (Eq. (9)), we build a Homotopy analysis method to resolve Eqs. (28) and (29) as shown in Box IV. Boundary circumstances are obtained by Eq. (30) as shown in Box V. We examine $f(\eta)$ and $\theta(\eta)$ in the following manner.

$$f(\eta) = f_0(\eta) + pf_1(\eta) + pf_2(\eta) + \cdots\cdots, \tag{31}$$

$$\theta(\eta) = \theta_0(\eta) + \theta_1(\eta) + \theta_2(\eta) + \cdots\cdots. \tag{32}$$

To replace Eqs. (23)-(25) with Eqs. (27)–(28), we get the following by contrasting the coefficient of indistinguishable powers of p terms and, then, setting the direct condition framework.

0th-order:

$$f_0 = \frac{n_1}{n_2}(1+2\eta\omega) f_0'' + \frac{n_1}{n_2}\left(\frac{(1+2\eta\omega)}{\gamma}\right) f_0''' = 0,$$

$$\theta_0 = \frac{4\omega\eta n_5}{Prn_4}\theta_0'' = 0. \tag{33}$$

With 0th request conditions:

$$f_0(0) = s, \qquad f_0'(0) = 1 + \left(1+\frac{1}{\gamma}\right)\delta f_0'',$$

$$f'(1) = 0, \quad \theta_0(0) = 1 + Bi\theta'(0), \quad \theta(1) = 0. \tag{34}$$

1st-order:

$$f_1 = 2\frac{n_1}{n_2}\omega\eta f_1''' + \frac{2\omega n_1 f_0''}{n_2\gamma} + \frac{2n_1\omega\eta f_1'''}{n_2\gamma} - {f'_0}^2 + \frac{n_1 f_1'''}{n_2\gamma} + \frac{2\omega n_1 f_0''}{n_2} - \frac{n_1 k f_0'}{\gamma} + \frac{n_1 f_1'''}{n_2} - n_3 M f_0' - n_1 k f_0' + f_0 f_0'' - Fr{f_0'}^2 = 0, \tag{35}$$

$$(1-p)\frac{n_1}{n_2}\left(1+\frac{1}{\gamma}\right)\left[(1+2\eta\omega) f'''\right] + p\begin{pmatrix} \frac{n_1}{n_2}\left(1+\frac{1}{\gamma}\right)\left[(1+2\omega\eta) f''' + 2\omega f''\right] + ff'' \\ -f'^2 - \left(\frac{n_3}{n_2}M + \frac{n_1}{n_2}\left(1+\frac{1}{\gamma}\right)k\right)f' - Frf'^2 \end{pmatrix} = 0, \tag{28}$$

$$(1-p)\left((1+2\eta\omega)\frac{1}{\mathrm{Pr}}\frac{n_5}{n_4} - \alpha_t f^2 - \frac{Rd}{n_4 Pr}(1+2\eta\omega)\right)\theta'' + p\begin{pmatrix} \frac{1}{Pr}\frac{n_5}{n_4}\left(2\theta'\omega + \theta''(1+2\eta\omega)\right) \\ -\frac{1}{Pr}\frac{1}{n_4}Rd\left(2\theta'\omega + \theta''(1+2\eta\omega)\right) \\ +\frac{n_3}{n_4}MEcf'^2 + \frac{n_1}{n_5}Ec\left(1+\frac{1}{\gamma}\right)(1+2\omega) f''^2 \\ -\alpha_t\left(\theta'' f^2 + ff'\theta'\right) + f\theta' + \frac{1}{n_4}Q\theta \end{pmatrix} = 0. \tag{29}$$

Box IV

$$\left.\begin{array}{ll} f(0) = s, f'(0) = 1 + \left(1+\frac{1}{\gamma}\right)\delta f''(0), n_5\theta'(0) = -Bi(1-\theta(0)) & \eta = 0 \\ f(\infty) \rightarrow 1; \theta(\infty) \rightarrow 0 & \eta \rightarrow \infty \end{array}\right\} \tag{30}$$

Box V

$$\theta_1 = \frac{n_5\theta_0''}{Prn_4} + \frac{n_1 Ecf_0''^2}{n_5} - \alpha_t f_0 f_0'\theta_0' - \frac{Rd\theta_0''}{Prn_4} + \frac{2n_1 Ec\eta\omega f_0''^2}{n_5\gamma} + \frac{Q\theta_0}{n_4} - \alpha_t\theta_0'' {f_0}^2 + f_0\theta_0' + \frac{4\omega\eta n_5\theta_1''}{Prn_4} - \frac{2\omega\eta n_5\theta_0''}{Prn_4} - \frac{2Rd\theta_0''\eta\omega}{Prn_4} + \frac{2n_1 Ec\eta\omega f_0''^2}{n_5} + \frac{n_3 MEcf_0'^2}{n_4} + \frac{n_1 Ecf_0''^2}{n_5\gamma} + \frac{2\omega n_5\theta_0'}{Prn_4} - \frac{2Rd\omega\theta_0'}{Prn_4} = 0. \tag{36}$$

Considering the 1st-order constraints:

$$f_1(0) = s, \qquad f_1'(0) = \left(1 + \frac{1}{\gamma}\right)\delta f_0''(0),$$

$$f_1'(1) = 0, \quad \theta_1(0) = Bi\theta_1'(0), \quad \theta_1(1) = 0. \tag{37}$$

2nd-order:

$$f_2 = \frac{2n_1\eta\omega f_2'''}{n_2} + \frac{2\omega n_1 f_1''}{n_2\gamma} + \frac{2n_1\eta\omega f_2'''}{n_2\gamma} + \frac{n_1 f_2'''}{n_2\gamma} + \frac{2\omega n_1 f_1''}{n_2} - \frac{n_1 kf_1'}{\gamma} + \frac{n_1 f_2'''}{n_2} - n_3 Mf' - n_1 k{f'}_1 - 2Frf_0'f_1' + f_0 f_1'' + f_1 f_0'' - 2f_0'f_1' = 0, \tag{38}$$

$$\theta_2 = \frac{4Ecn_1\eta\omega f_0''f_1''}{n_5\gamma} + f_0\theta_1' + f_1\theta_0' + \frac{n_5\theta_1''}{Prn_4} - 2\alpha_t\theta_0'' f_0 f - \alpha_t f_0 f_0'\theta_1' - \alpha_t f_0 f'\theta_0' - \alpha_t f_1 f_0'\theta_0' - \frac{Rd\theta_1''}{Prn_4} + \frac{4n_1 Ec\eta\omega f_0''f_1''}{n_5} + \frac{Q\theta_1}{n_4} - \alpha_t{\theta''}_1{f_0}^2 + \frac{2\omega n_5\theta_1'}{Prn_4} - \frac{2Rd\omega\theta_1'}{Prn_4} + \frac{2n_1 Ecf_0''f_1''}{n_5} + \frac{4n_5\eta\omega\theta_2''}{Prn_4} - + \frac{2n_5\omega\eta\theta_1''}{Prn_4} + \frac{2n_3 MEcf_0'f_1'}{n_4} - \frac{2Rd\omega\eta\theta_1''}{Prn_4} + \frac{2n_1 Ecf_0''f_1''}{n_5\gamma} = 0. \tag{39}$$

Consider the 2nd-order constraint:

$$f_2(0) = s, \quad f_2'(0) = \left(1 + \frac{1}{\gamma}\right)\delta f_2''(0),$$

$$f_2'(1) = 0, \quad \theta_2(0) = \theta_2(0) = 1 + Bi\theta_2',$$

$$\theta_2(1) = 0. \tag{40}$$

4. Results and discussion

The current study investigates the behavior of a porous medium and Darcy-Forchheimer flow of Ag-TiO_2/blood owing a starching cylinder under a variety of situations, including velocity slip, thermal radiation, Casson fluid, a convective boundary condition, and Cattaneo-Christov heat flux. To obtain the required solution to the updated nonlinear coupled equations, the bvp4c approach was used. The effects of non-dimensional governing parameters on f' (velocity) and θ (temperature) profiles, N_G (entropy generation), and the Be (Bejan number), as well as the $1/2C_f Re_x^{1/2}$ (skin-friction) and $Nu_x Re_x^{-1/2}$ (local Nusselt numbers), can be illustrated in the results. The current analysis establishes universal values for the following parameters:

$$\omega = 0.5, \quad M = 0.7, \quad \gamma = 2.5, \quad k = 0.5, \quad Pr = 21,$$

$$\alpha_t = 0.02, \quad Ec = 0.03, \quad Rd = 0.6, \quad s = 0.05$$

$$Q = 0.3, \quad \alpha_1 = 0.01, \quad Br = 0.04, \quad \delta = 0.01,$$

$$Bi = 0.1, \quad Re = 0.01, \quad X = 0.01.$$

Table 3 shows that the numerical result for the parameter magnetic field in NM corresponding to the HPM in Maple is compared. Figures 2 to 5 compare the homotopy perturbation approach with the numerical method. In comparison to the numerical technique, the HPM enjoys high precision for the following values:

$$\omega = 0.5, M = 0.5, \quad \gamma = 2.5, \quad k = 0.5, \quad Pr = 21,$$

$$\alpha_t = 0.02, \quad Ec = 0.03, \quad Rd = 0.6, \quad s = 0.02,$$

$$Q = 0.3, \quad \alpha_1 = 0.01, \quad Br = 0.4, \quad \delta = 0.01,$$

$$Bi = 0.1, \quad Re = 0.01, \quad X = 0.1.$$

Table 3. Comparison of the numerical outcomes off $f'''(0)$ for different values of MN when $\omega = 0$ [47].

M	Vajravelu et al. [47]		Present	
	Numerical solution by Keller-box method	Analytical solution	HPM	NM
0	1.000001	1.000000	1.000003	1.000008
0.5	1.224745	1.224745	1.224745	1.224744
1	1.414214	1.414214	1.414214	1.414213
1.5	1.581139	1.581139	1.581139	1.581138
2	1.732051	1.732051	1.732051	1.732050

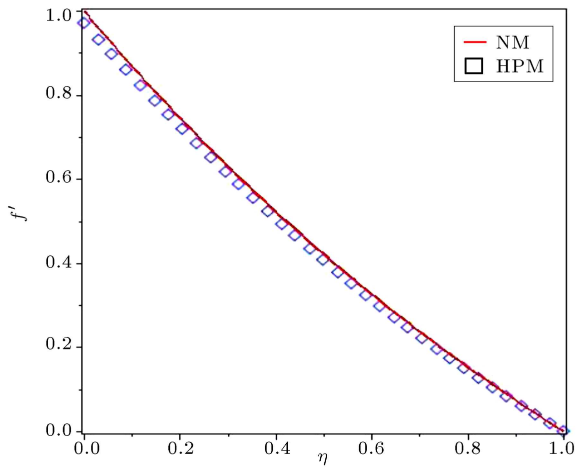

Figure 2. Comparison between NM and HPM for NG.

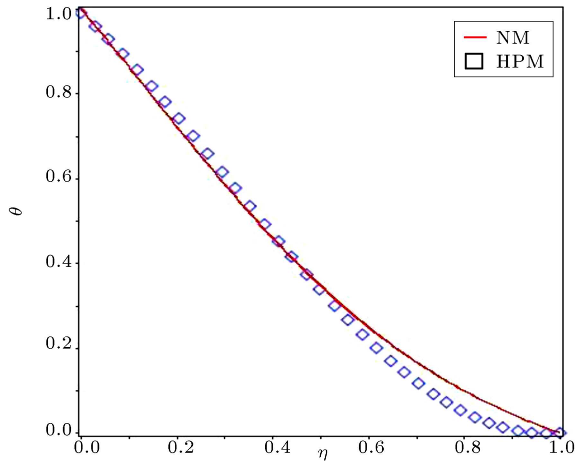

Figure 3. Comparison between NM and HPM for NG.

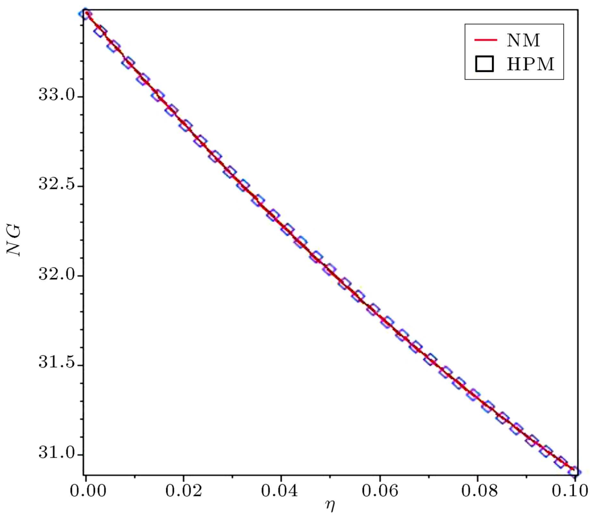

Figure 4. Comparison between NM and HPM for NG.

There are no deviations from these numbers across the whole research except for those in the individual figures and tables. Dashed and solid lines represent the Newtonian and non-Newtonian fluids, respectively, in graphical results.

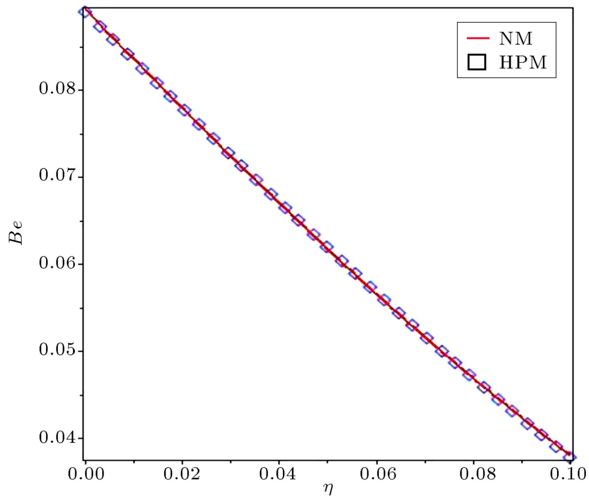

Figure 5. Comparison between NM and HPM for NG.

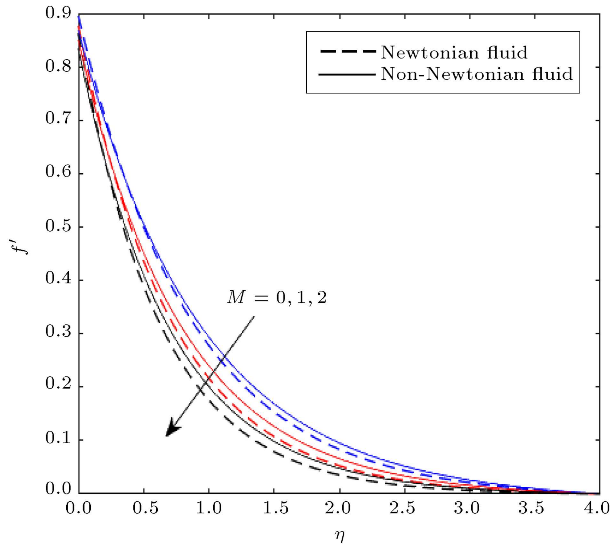

Figure 6. Impact of M on f'.

Figure 6 depicts the effect of magnetic parameter M on the radial velocity profile f' for various combinations of the Ag-TiO_2/blood mixture. It is demonstrated that the radial velocity of the liquid decreases with increasing values of the magnetic parameter M. These results are consistent with the fact that the resistive force is important in deceleration and directional fluid flow. A magnetic parameter (M) has a strong physical relationship with the resistive field, which is known as the Lorentz force. The speed profiles over the boundary layer go down because the value of M goes up. The greater the Lorentz force, which slows the fluid's velocity inside the boundary layer, the higher the magnetic parameter (M) value. The effect of the porosity on velocity variation in Newtonian and non-Newtonian cases is depicted in Figure 7, as illustrated in Figure 7. It is implied that rise in the porosity reduces the fluid velocity profile and boundary layer.

Figure 8 represents the characteristics of (M)

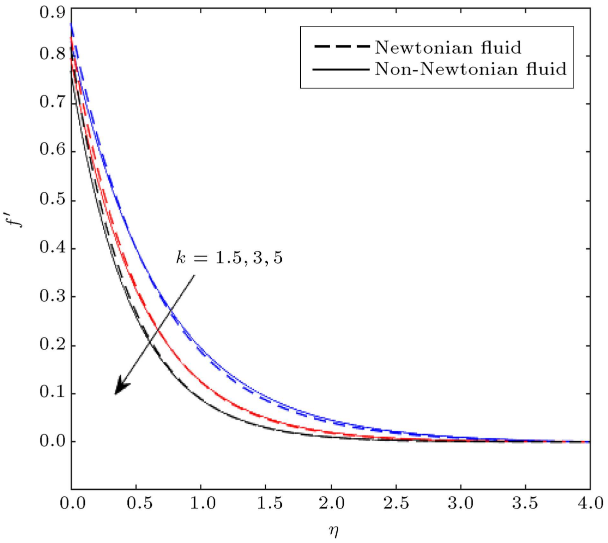

Figure 7. Impact of k on f'.

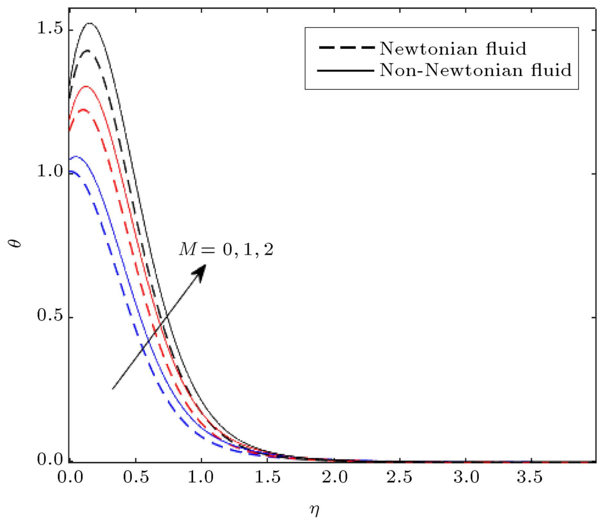

Figure 8. Impact of M on θ.

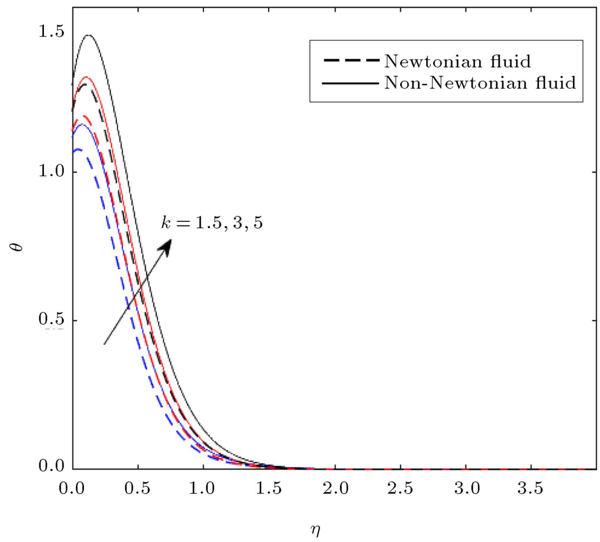

Figure 9. Impact of k on θ.

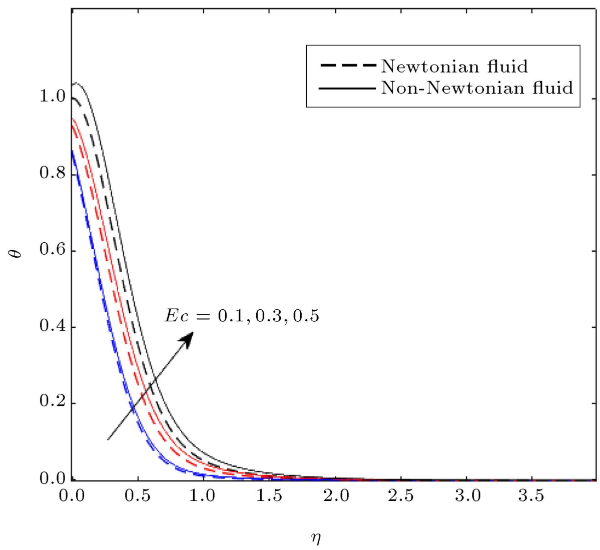

Figure 10. Impact of Ec on θ.

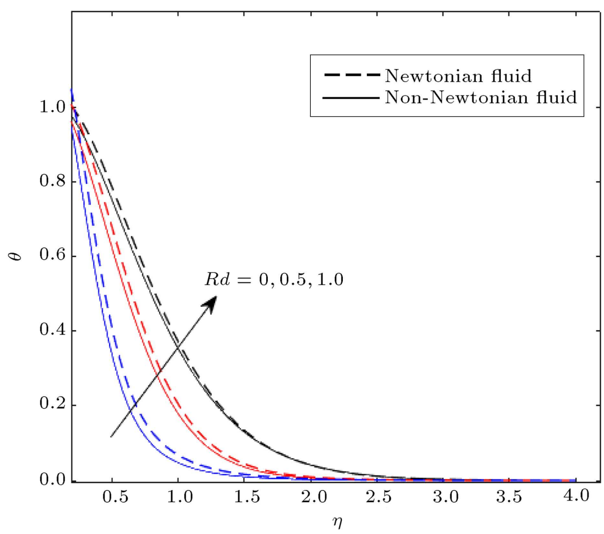

Figure 11. Impact of Rd on θ.

magnetic field effects on temperature field $\theta(\eta)$. The increase in magnetic strength on the liquid flow generates friction, which produces some amount of heat and as a result, the normal temperature of the liquid rises. Figure 9 depicts the behavior of the temperature profile $\theta(\eta)$ in both Newtonian and non-Newtonian cases. As the k value increases, temperature profile $\theta(\eta)$ acquires more heat by increasing its tendency. Figure 10 depicts the increasing results of temperature at higher values of Eckert number. As a result of frictional heating, extra kinetic energy is stored in the fluid particles, resulting in the temperature outcome. Thus, the temperature field increases as the Eckert number (Ec) increases. Figure 11 shows that by rising the radiation parameter, temperature profile rises gradually. Figure 12 demonstrates that as α_t increases, the temperature profile decreases for the both Newtonian and non-Newtonian cases.

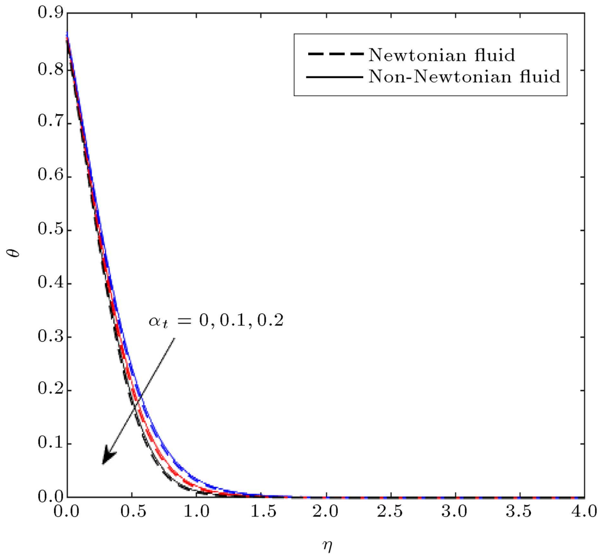

Figure 12. Impact of α_t on θ.

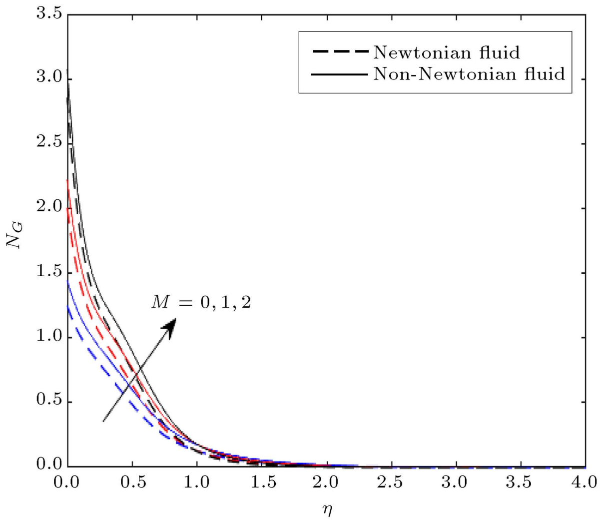

Figure 13. Impact of M on N_G.

The rising upside of the entropy generation N_G with increase in the magnetic field M parameter is observed from Figure 13. The Lorentz force increases the strength; as a result, the magnetic boundary M becomes larger. Figure 14 shows that as the Brinkman number Br increases, the rate of entropy generation N_G rises. The current situation in entropy generation rate results from the fact that thick impacts have become more pronounced with increase in Brinkman number in both Newtonian and non-Newtonian cases.

Figure 15 shows the difference in Bejan number (Be) profile caused by different values. For both non-Newtonian and Newtonian scenarios, following increase in the M values, the Bejan number (Be) profile increases. Figure 16 recommends that at a greater Brinkman number, Bejan number reductions are observed for both non-Newtonian and Newtonian cases.

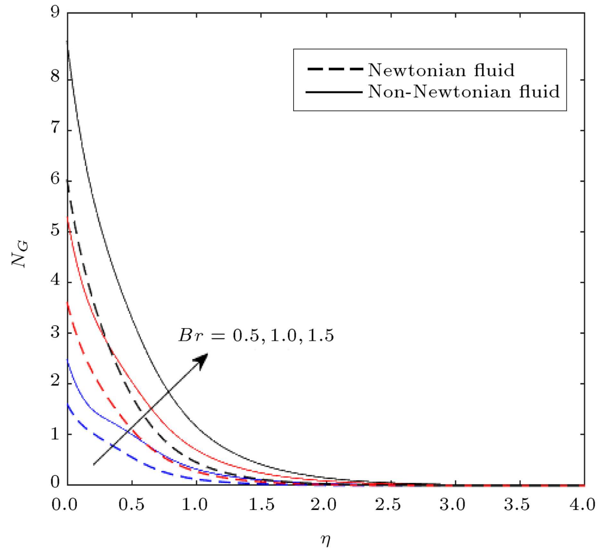

Figure 14. Impact of Br on N_G.

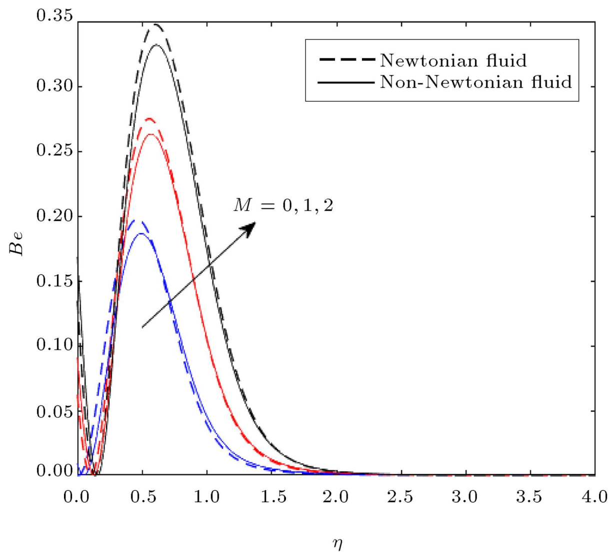

Figure 15. Impact of M on Be.

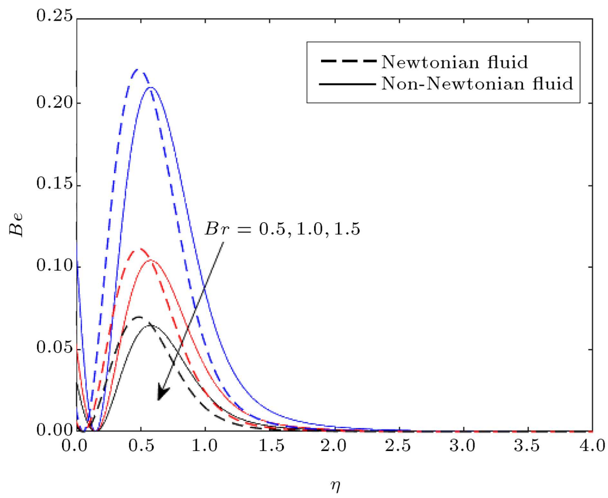

Figure 16. Impact of Br on Be.

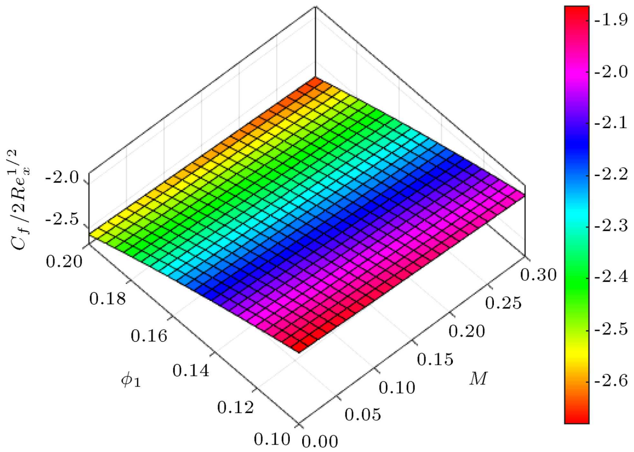

Figure 17. Impact of ϕ_1 and M on $C_f/2\sqrt{Re_x}$.

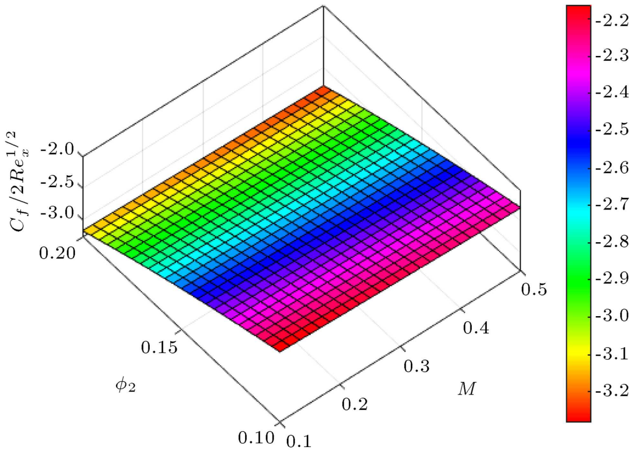

Figure 18. Impact of ϕ_2 and M on $C_f/2\sqrt{Re_x}$.

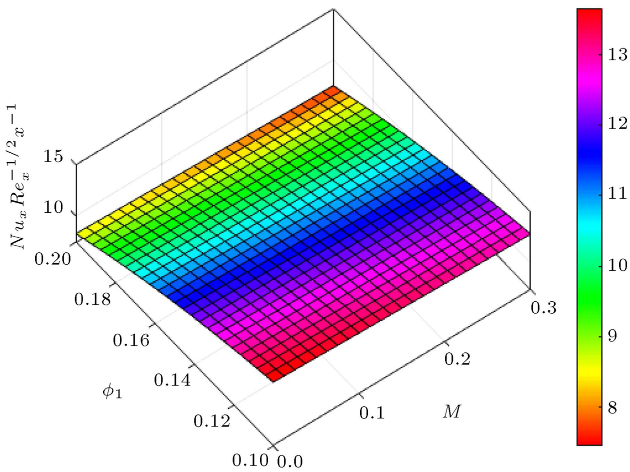

Figure 19. Impact of ϕ_1 and M on $Nu_x Re_x^{-1/2}$.

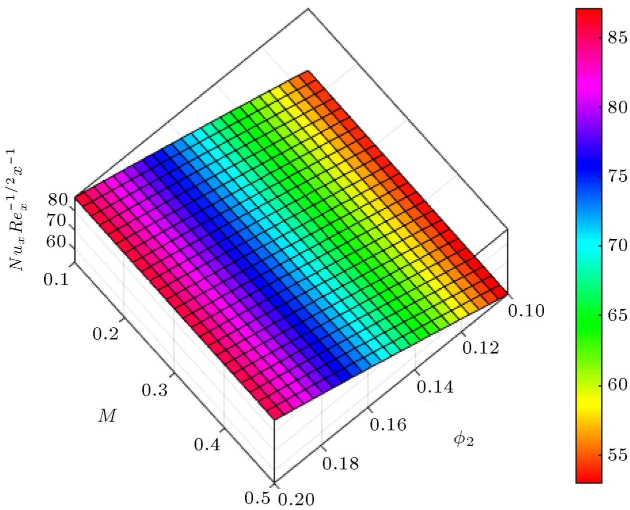

Figure 20. Impact of ϕ_2 and M on $Nu_x Re_x^{-1/2}$.

Figures 17 and 18 show the behavior of $1/2C_f Re_x^{1/2}$ coefficient for various parameters like magnetic field and volume fractions ϕ_1 and ϕ_2. The conducting of magnetic field and volume fractions of ϕ_1 and ϕ_2 on skin friction coefficient $1/2C_f Re_x^{1/2}$ is shown in Figures 17 and 18. Figures 19 and 20 show the behavior of $Nu_x Re_x^{1/2}$ coefficient for various approximations of the ratio of velocities and magnetic field (M), as well as volume fractions ϕ_1 and ϕ_2. According to Figures 19 and 20, it can be realized that $Nu_x Re_x^{1/2}$ decreases when the upsides of magnetic field of volume fraction ϕ_1 rise, although the opposing inclination is seen on account of magnetic field M and volume fraction ϕ_2, which can be found in Figure 20.

5. Conclusion

The current study examined blood flow through a stretching cylinder for drug delivery through a porous medium using MHD. The Darcy-Forchheimer, Cattaneo-Christov heat flux model, heat generation/absorption parameter, Eckert number, porosity parameter, and radiation parameter results were all taken into account. It was discovered that the properties of TiO_2 and Ag had valuable antimicrobial recognition and that they could be used in an Escherichia coli culture to evaluate their antibacterial viewpoint. In medicine, TiO_2 and Ag hybrid nanofluids are used because they have a high pH value resulting from temperature changes. In the first step, the governing PDEs were converted into a system of ODEs and then, solved numerically by the bvp4c method. Graphs were used to investigate the changes in velocity, temperature, entropy, Bejan number, skin friction coefficient, and Nusselt number caused by changes in physical parameters. The comparison graphs and tables for NM and HPM methods were also included in this paper. The main findings of the current study are given in the following:

- One of the best nanocomposites for use in the blood is made of TiO_2 titanium dioxide and Ag silver, because they can stop bacteria from growing and stop new cells from forming, making them ideal for use in blood;

- In both cases of Newtonian or non-Newtonian, the values of magnetic and porosity parameters increase as the velocity decreases;
- Temperatures rise when a large number of factors including M, k, and Ec are involved. This finding holds for hybrid nanofluids, which are made up of many different types of nanofluids. Furthermore, the increasing values of Rd and α_t result in a decrease in the temperature field;
- The entropy generation profile is improved on account of a rise in M and Br parameters. As the Bejan number and magnetic parameter value increase, the Brinkmen number decreases;
- While increasing the wall slip parameter increases the skin friction factor, increasing the porosity parameter decreases the skin friction coefficient;
- The above phenomenon helps Escherichia coli grow; hence, TiO_2 and Ag hybrid nanofluids exhibit proper performance to kill germs;
- The electric conductivity and pH values improve with the higher amount of heat transfers. Therefore, the objective of this study was to use the TiO_2 + Ag nanofluids for medicine.

Nomenclature

A	Radius of a cylinder (m)
U_0	Reference velocity (m/s)
B_0	Magnetic field ($Nm^{-1}A^{-1}$)
Br	Brownian motion
Fr	Inertia coefficient
Ec	Eckert number
M	Magnetic field
h	Mass flux vector
h_w	Surface mass flux of Casson fluid
l	Characteristic length (m)
N	Number of collocation points
u, v	Velocity components (m/s)
T_w	Wall temperature (K)

Greek symbols

α	Variable thermal diffusivity (m^2/s)
α_t	Temperature time relaxation parameter
α_{ij}	Rate of strain tenser
α_∞	Ambient fluid thermal diffusivity (m^2/s)
δ	Velocity slip parameter
δ_t	Thermal slip factor
ε	Variable thermal conductivity parameter
υ	Kinematic viscosity of fluid (m^2/s)
λ_e	Relaxation time of heat flux ω (seconds)
π	Product of deformation rate tensor
T_∞	Ambient temperature (K)
S_G	Characteristic entropy generation rate
S_0	Entropy generation number
Re_x	Local Reynolds number
Pr	Prandtl number
u_w	Linear axial velocity (m/s)
k	Permeability of porous medium
k	Thermal conductivity ($Wm^{-1}K^{-1}$)
N_G	Dimensionless form of entropy generation
Nu_x	Local Nusselt number
T_0	Reference temperature (K)
s	Suction/blowing parameter
S'''_{gen}	Characteristic entropy generation rate
ρ	Density of Casson nanofluid (km/m^3)
k	Permeability parameter of porous media
θ	Dimensionless temperature
ψ	Stream function
γ	Non-Newtonian Casson parameter
η	Variable of dimensionless
τ	Ratio of effective heat capacity
τ_w	Surface shear stress of Casson fluid
ω	Curvature parameter

References

1. Hayat, T., Asad, S., and Alsaedi, A. "Flow of variable thermal conductivity fluid due to inclined stretching cylinder with viscous dissipation and thermal radiation", *Applied Mathematics and Mechanics* (English Edition), **35**(6), pp. 717–728 (2014).
2. Ullah, I., Alkanhal, T.A., Shafie, S., et al. "MHD slip flow of Casson fluid along a nonlinear permeable stretching cylinder saturated in a porous medium with chemical reaction, viscous dissipation, and heat generation/absorption", *Symmetry*, **11**(4), p. 531 (2019).
3. Alwawi, F.A., Alkasasbeh, H.T., Rashad, A.M., et al. "Heat transfer analysis of ethylene glycol-based Casson nanofluid around a horizontal circular cylinder with MHD effect", *Proceedings of the Institution of Mechanical Engineers, Part C: Journal of Mechanical Engineering Science*, **234**(13), pp. 2569–2580 (2020).
4. Sakkaravarthi, K. and Bala Anki Reddy, P. "Entropy generation on Casson hybrid nanofluid over a curved stretching sheet with convective boundary condition: Semi-analytical and numerical simulations", *Proceedings of the Institution of Mechanical Engineers, Part*

C: Journal of Mechanical Engineering Science (2022). https://doi.org/10.1177/09544062221119055

5. Ramasekhar, G. and Bala Anki Reddy, P. "Entropy generation on EMHD Darcy-Forchheimer flow of Carreau hybrid nano fluid over a permeable rotating disk with radiation and heat generation: Homotopy perturbation solution", *Proceedings of the Institution of Mechanical Engineers, Part E: Journal of Process Mechanical Engineering* (2022). https://doi.org/10.1177/09544089221116575

6. Chamkha, A.J. and Rashad, A.M. "Unsteady heat and mass transfer by MHD mixed convection flow from a rotating vertical cone with chemical reaction and Soret and Dufour effects", *Canadian Journal of Chemical Engineering*, **92**(4), pp. 758–767 (2014).

7. Nadeem, S. and Saleem, S. "Unsteady mixed convection flow of nanofluid on a rotating cone with magnetic field", *Applied Nanoscience (Switzerland)*, **4**(4), pp. 405–414 (2014).

8. Dhanai, R., Rana, P., and Kumar, L. "MHD mixed convection nanofluid flow and heat transfer over an inclined cylinder due to velocity and thermal slip effects: Buongiorno's model", *Powder Technology*, **288**, pp. 140–150 (2016).

9. Khan, M.I., Tamoor, M., Hayat, T., et al. "MHD boundary layer thermal slip flow by nonlinearly stretching cylinder with suction/blowing and radiation", *Results in Physics*, **7**, pp. 1207–1211 (2017).

10. Patil, P.M., Kulkarni, M., and Tonannavar, J.R. "Influence of applied magnetic field on nonlinear mixed convective nanoliquid flow past a permeable rough cone", *Indian Journal of Physics,* **2021**, pp. 1–12 (2021).

11. Isa, S.S.P.M., Arifin, N.M., Nazar, R., et al. "MHD mixed convection boundary layer flow of a Casson fluid bounded by permeable shrinking sheet with exponential variation", *Scientia Iranica*, **24**(2), pp. 637–647 (2017).

12. Atif, S.M., Shah, S., and Kamran, A. "Effect of MHD on Casson fluid with Arrhenius activation energy and variable properties", *Scientia Iranica*, **29**(6) (2021). Doi:10.24200/SCI.2021.57873.5452

13. Shahzad, F., Sagheer, M., Hussain, S. "Transport of MHD nanofluid in a stratified medium containing gyrotactic microorganisms due to a stretching sheet", *Scientia Iranica, F*, **28**(6), pp. 3786–3805 (2021).

14. Sheikholeslami, M., Jalili, P., and Ganji, D.D. "Magnetic field effect on nanofluid flow between two circular cylinders using AGM", *Alexandria Engineering Journal*, **57**(2), pp. 587–594 (2018).

15. Abbasi, F.M., Mustafa, M., Shehzad, S.A., et al. "Analytical study of Cattaneo-Christov heat flux model for a boundary layer flow of Oldroyd-B fluid", *Chinese Physics*, **25**(1), 014701 (2015).

16. Khan, J.A., Mustafa, M., Hayat, T., et al. "Numerical study of cattaneo-christov heat flux model for viscoelastic flow due to an exponentially stretching surface", *PLoS ONE*, **10**(9), e0137363 (2015).

17. Akbar, N.S., Khalique, C., and Khan, Z.H. "Cattanneo-Christov heat flux model study for water-based CNT suspended nanofluid past a stretching surface", In *Nanofluid Heat and Mass Transfer in Engineering Problems* (2017). http://dx.doi.org/10.5772/65628

18. Cattaneo, C. "Sulla conduzione del calore", *Atti Sem. Mat. Fis. Univ. Modena*, **3**, pp. 83–101 (1948).

19. Christov, C.I. "On frame indifferent formulation of the Maxwell-Cattaneo model of finite-speed heat conduction", *Mechanics Research Communications*, **36**(4), pp. 481–486, Elsevier (2009).

20. Tibullo, V. and Zampoli, V. "A uniqueness result for the Cattaneo-Christov heat conduction model applied to incompressible fluids", *Mechanics Research Communications*, **38**(1), pp. 77–79 (2011).

21. Kumar, K.A., Reddy, J.R., Sugunamma, V., et al. "Magnetohydrodynamic Cattaneo-Christov flow past a cone and a wedge with variable heat source/sink", *Alexandria Engineering Journal*, **57**(1), pp. 435–443 (2018).

22. Kundu, P.K., Chakraborty, T., and Das, K. "Framing the Cattaneo-Christov heat flux phenomena on CNT-based maxwell nanofluid along stretching sheet with multiple slips", *Arabian Journal for Science and Engineering*, **43**(3), pp. 1177–1188 (2018).

23. Shahid, M.I., Ahmad, S., and Ashraf, M. "Simulation analysis of mass and heat transfer attributes in nanoparticles flow subject to Darcy-Forchheimer medium", *Scientia Iranica*, **29**(4), pp. 1828–1837 (2022). DOI: 10.24200/SCI.2022.58552.5786

24. Jakeer, S. and Polu, B.A.R. "Homotopy perturbation method solution of magneto-polymer nanofluid containing gyrotactic microorganisms over the permeable sheet with Cattaneo-Christov heat and mass flux model", *Proceedings of the Institution of Mechanical Engineers, Part E: Journal of Process Mechanical Engineering*, **236**(2), pp. 525–534 (2022).

25. Bejan, A. "Second law analysis in heat transfer", *Energy*, **5**(8–9), pp. 720–732 (1980).

26. Khan, N., Riaz, I., Hashmi, M.S., et al. "Aspects of chemical entropy generation in flow of Casson nanofluid between radiative stretching disks", *Entropy*, **22**(5), p. 495 (2020).

27. Rashidi, M.M., Abelman, S., and Mehr, N.F. "Entropy generation in steady MHD flow due to a rotating

porous disk in a nanofluid", *International Journal of Heat and Mass Transfer*, **62**(1), pp. 515–525 (2013).

28. Han, S., Zheng, L., Li, C., et al. "Coupled flow and heat transfer in viscoelastic fluid with Cattaneo-Christov heat flux model", *Applied Mathematics Letters*, **38**, pp. 87–93 (2014).

29. Aziz, A. and Shams, M. "Entropy generation in MHD Maxwell nanofluid flow with variable thermal conductivity, thermal radiation, slip conditions, and heat source", *AIP Advances*, **6**(3) (2020).

30. Mburu, Z.M., Mondal, S., and Sibanda, P. "Numerical study on combined thermal radiation and magnetic field effects on entropy generation in unsteady fluid flow past an inclined cylinder", *Journal of Computational Design and Engineering*, **8**(1), pp. 149–169 (2021).

31. Rashid, M., Hayat, T., and Alsaedi, A. "Entropy generation in Darcy-Forchheimer flow of nanofluid with five nanoarticles due to stretching cylinder", *Applied Nanoscience*, **9**(8), pp. 1649–1659 (2019).

32. Hayat, T., Khan, S.A., Ijaz Khan, M., et al. "Irreversibility characterization and investigation of mixed convective reactive flow over a rotating cone", *Computer Methods and Programs in Biomedicine*, **185**, p. 105168 (2020).

33. Eswaramoorthi, S. and Sivasankaran, S. "Entropy optimization of MHD Casson-Williamson fluid flow over a convectively heated stretchy sheet with Cattaneo-Christov dual flux", *Scientia Iranica*, **29**(5), pp. 2317–2331 (2022).

34. Vijatha, M. and Reddy, P.B.A. "Entropy optimization on MHD flow of Williamson hybrid nanofluid with Cattaneo-Christov heat flux: A comparative study on stretching cylinder and sheet Entropy optimization on MHD flow of Williamson hybrid nanofluid with Cattaneo-Christov heat flux", *Waves in Random and Complex Media*, pp. 1-32 (2022). https://doi.org/10.1080/17455030.2022.2094029

35. Kardri, M.A., Bachok, N., Arifin, N., et al., *Magnetohydrodynamic Flow Past a Nonlinear Stretching or Shrinking Cylinder in Nanofluid with Viscous Dissipation and Heat Generation Effect*, **1**(1), pp. 102–114 (2022).

36. Yin, J., Zhang, X., Israr Ur Rehman, M., et al. "Thermal radiation aspect of bioconvection flow of magnetized Sisko nanofluid along a stretching cylinder with swimming microorganisms", *Case Studies in Thermal Engineering*, **30**, p. 101771 (2022).

37. Wu, J., Wu, F., Zhao, T., et al. "Dual-band nonreciprocal thermal radiation by coupling optical Tamm states in magnetophotonic multilayers", *International Journal of Thermal Sciences*, **175**, 107457 (2021).

38. Jalili, B., Ghafoori, H., and Jalili, P. "Investigation of carbon nano-tube (CNT) particles effect on the performance of a refrigeration cycle", *International Journal of Material Science Innovations*, **2**(1), pp. 8–17 (2014).

39. Talarposhti, R.A., Jalili, P., Rezazadeh, H., et al. "Optical soliton solutions to the (2 + 1)-dimensional Kundu-Mukherjee-Naskar equation", *International Journal of Modern Physics B*, **34**(11), pp. 1–15 (2020).

40. Ali, M., Shahzad, M., Sultan, F., et al. "Numerical analysis of chemical reaction and non-linear radiation for magneto-cross nanofluid over a stretching cylinder", *Applied Nanoscience*, **10**(8), pp. 3259–3267 (2020).

41. Mitri, F.G. "Acoustic radiation force on a cylindrical particle near a planar rigid boundary II. - Viscous fluid cylinder example and inherent radiation torque", *Physics Open*, **4**(May), p. 100029 (2020).

42. Saharian, A.A., Kotanjyan, A.S., Grigoryan, L.S., et al. "Synchrotron radiation from a charge circulating around a cylinder with negative permittivity", *International Journal of Modern Physics B*, **34**(8), pp. 1–16 (2020).

43. Yahyazadeh, H., Ganji, D.D., Yahyazadeh, A., et al. "Evaluation of natural convection flow of a nanofluid over a linearly stretching sheet in the presence of magnetic field by the differential transformation method", *Thermal Science*, **16**(5), pp. 1281–1287 (2012).

44. Tulu, A. and Ibrahim, W. "Spectral relaxation method analysis of Casson nanofluid flow over stretching cylinder with variable thermal conductivity and Cattaneo–Christov heat flux model", *Heat Transfer*, **49**(6), pp. 3433–3455 (2020).

45. Khashi'ie, N.S., Arifin, N.M., Pop, I., et al. "Flow and heat transfer of hybrid nanofluid over a permeable shrinking cylinder with Joule heating: A comparative analysis", *Alexandria Engineering Journal*, **59**(3), pp. 1787–1798 (2020).

46. Saleem, N., Munawar, S., and Tripathi, D. "Entropy analysis in ciliary transport of radiated hybrid nanofluid in presence of electromagnetohydrodynamics and activation energy", *Case Studies in Thermal Engineering*, **28**(August), p. 101665 (2021).

47. Vajravelu, K., Prasad, K.V., and Santhi, S.R. "Axisymmetric magneto-hydrodynamic (MHD) flow and heat transfer at a non-isothermal stretching cylinder", *Applied Mathematics and Computation*, **219**(8), pp. 3993–4005 (2012).

Biographies

M. Vijatha is pursuing her PhD program at Vellore Institute of Technology, Vellore, Tamilnadu, India. She completed her MSc in the year 2016 at SPMVV University, Tirupati, Andhra Pradesh, India. Her research interests are fluid dynamics, heat transfer,

boundary-layer theory.

Polu Bala Anki Reddy was born and brought up in Andhra Pradesh, India. He obtained the MSc and PhD degrees in Mathematics from the Sri Venkateswara University, Tirupati, Andhra Pradesh. Presently, he is working as an Associate Professor at the Department of Mathematics, Vellore Institute of Technology, Vellore, Tamilnadu. Dr. Reddy's research interest covers the application of flow separation, particularly in bio-fluid dynamics and analysis of boundary layer flows of Newtonian/non-Newtonian fluids including entropy generation. His research interest also covers the hybrid nanofluid flow with entropy generation. He has published several papers in national and international journals and attended several workshops/seminars/faculty development programs. Moreover, Reddy has been selected as the top 2% of scientists in the world by Stanford University, USA, and Elsevier BV for the year 2022.